Bulletin of the Seismological Society of America, Vol. 95, No. 1, pp. 159–172, February 2005, doi: 10.1785/0120040035

Ⓔ

Iterative Deconvolution of Regional Waveforms and a Double-Event Interpretation of the 2003 Lefkada Earthquake, Greece

by Jiří Zahradník, Anna Serpetsidaki, Efthimios Sokos, and G-Akis Tselentis

Abstract The moment tensor inversion for multiple point sources, based on Kikuchi and Kanamori (1991), was extended to full waveform data at regional (or local) distances. The new code proved to be efficient for retrieving major source contributions of the 2003 Lefkada, Greece, earthquake. The source model was derived from five three-component regional stations (epicentral distances <140 km), at periods 10–20 s. Two main events dominated the rupture process, one at the Lefkada Island (comprising three subevents of total moment 0.9×10^{18} N m) and the other at the Cephalonia Island (comprising one subevent of 0.5×10^{18} N m). Their spatial and temporal separation is 40 km and 14 s, respectively. They can be understood as two earthquakes. The uncertainty estimate based on reduced data sets (repeatedly excluding a station) shows that the Cephalonia subevent and the major Lefkada subevent are very well resolved regarding their position, time, and focal mechanism. The source model explains well the aftershock distribution, characterized by two clusters at the Lefkada and Cephalonia Islands, respectively. The focal mechanisms of the two main subevents are predominantly right-lateral strike slip of south-southwest–north-northeast orientation. The Cephalonia subevent occurred on a less steeply dipping fault with a small thrust component. Large deviations from pure double couple were found but interpreted as artifacts. The new software developed in this article (Fortran code and Matlab graphic user interface) is freely available.

Online material: Color graphics and 3D visualization of the 2003 Lefkada earthquake sequence.

Introduction

The Ionian Islands (e.g., Zakynthos, Cephalonia, Lefkada, and Corfu) belong to the most seismically active regions of the Mediterranean. The Cephalonia transform fault (Fig. 1) in the transition between Hellenic subduction to the south and continental collision to the north is a major feature dominated by right-lateral strike-slip motion. The northern part of the Cephalonia transform fault, the so-called Lefkada Fault Segment, following the western coast of Lefkada Island, is striking north-northeast and dipping east, and its length is about 40 km. At least 15 events of a magnitude greater than 6 have occurred close to Lefkada since the seventeenth century; the largest events of the last century were *M* 6.3 on 27 November 1914 and *M* 6.5 on 22 April 1948. For details, see Papazachos and Papazachou (1997), Louvari *et al.* (1999), and Papadimitriou (2002) and references therein.

This article studies the most recent *M* 6 event on Lefkada, the earthquake of 14 August 2003 (at 05:14:54 UTC) (see Table 1). The main objective is to study the source process and to explain the specific aftershock pattern, dominated by two spatially separated clusters.

Source inversions seeking for space-time variation of slip on a rectangular fault are often inherently nonunique and require additional constraints (Das and Kostrov, 1990). Because the slip is usually concentrated in very few areas of the fault (Somerville *et al.*, 1999), a reasonable strategy is to seek just those areas. Promising methods of that kind are the so-called patch inversion (Valee and Bouchon, 2004) or the iterative deconvolution of multiple point sources (Kikuchi and Kanamori, 1991). The latter method has been chosen for this study, because it also enables retrieval of the space-time varying moment tensor. The method inspects a set of predefined point-source positions, that is, "slip candidates," distributed along a fault plane or a line. Because the source inversions usually have worse resolution along dip than along strike (Lavalee and Archuleta, 2003), we study only a linear horizontal array of the potential source positions. For a similar philosophy, see, for example, Frankel (2003) and Kuge (2003).

We extend the Kikuchi and Kanamori (1991) technique from teleseismic to regional or local data. To this goal, we

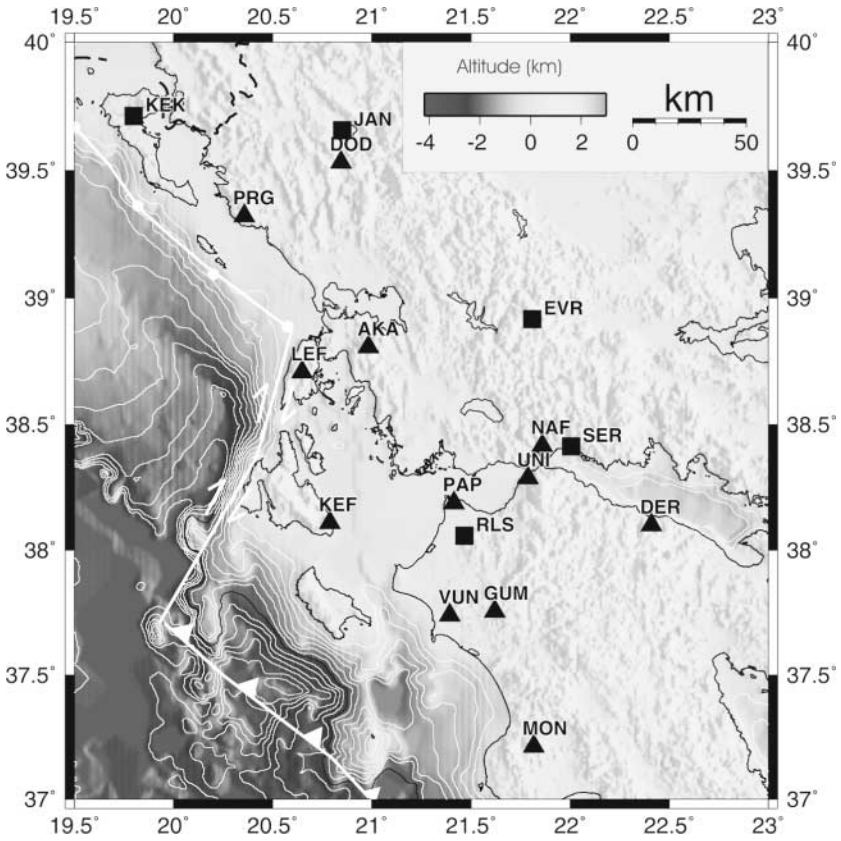

Figure 1. Western Greece, major faults, and seismic stations. Hellenic subduction (line with teeth), the Cephalonia transform fault (arrows), and the continental collision (line with dots) are shown. The PATNET short-period stations used in location are denoted by triangles. The broadband stations used in the waveform inversion are denoted by squares. (Ⓔ A color version of this figure is available online at the SSA Web site.)

Table 1
Basic Parameters of the 14 August 2003 Lefkada Earthquake as Reported by Several Agencies

Agency	Latitude N (°)	Longitude E (°)	Depth (km)	Moment (10^{18} N m)	Strike (°)	Dip (°)	Rake (°)
USGS	39.16	20.61	21	2.0	13	84	172
Harvard	38.70	20.67	15	3.0	18	59	−174
MEDNET	38.88	20.62	24	2.6	196	85	−166
SED	39.16	20.61	21	4.1	14	69	174

SED denotes the seismic service of Switzerland.

developed a completely new computer code, allowing full wavefield inversion, based on the discrete wavenumber method of Bouchon (1981) and Coutant (1989). A useful part of the code is an interactive graphical tool with which various constraints can be applied during inversion, such as the first-motion polarity constraint, constraint of the fault-dipping direction, constraint of the rupture velocity, etc. Extensive numerical tests of the new code on regional waveforms (<140 km) of the 2003 Lefkada *M* 6 earthquake were performed focusing mainly on the uncertainty and resolution. More specifically, we will show that two major subevents of this earthquake (separated by nearly 40 km) are stable and well resolved, but the uncertainty increases when proceeding to additional smaller subevents. Thus, only four subevents will be reported. Because most tests were performed in parallel with an unconstrained (deviatoric) moment tensor and the double couple (DC)-constrained moment tensor, we were able to clearly detect the spurious character of the non-DC (CLVD) components. Therefore, we present only the DC-constrained moment tensors. Finally, we discuss the segmented nature of the mainshock and suggest its interpretation as two earthquakes.

Location

The mainshock and about 470 aftershocks (14–30 August 2003) were located by using records of the short-period telemetered network of the Patras University (PATNET). The HYPO71PC code of Lee and Valdés (1989) was used in three 1D crustal models, those of Tselentis *et al.* (1996), Haslinger *et al.* (1999), and Novotný *et al.* (2001). The model of Novotný *et al.* (2001) provided nonrealistic shallow depths, accompanied by the largest depth errors, so it is not discussed further. The other two models provided similar location results, but the model by Haslinger *et al.* (1999) allowed more realistic waveform modeling. Therefore, it was used in this article both for location and for the waveform modeling. In Figure 2, the locations are shown for 288 events with at least five arrival-time readings, rms <0.4 s, and erh, erz <10 km. The mainshock coordinates are listed in Table 2.

The major fault of the studied zone, the Cephalonia transform fault, consists of two parts of a slightly different

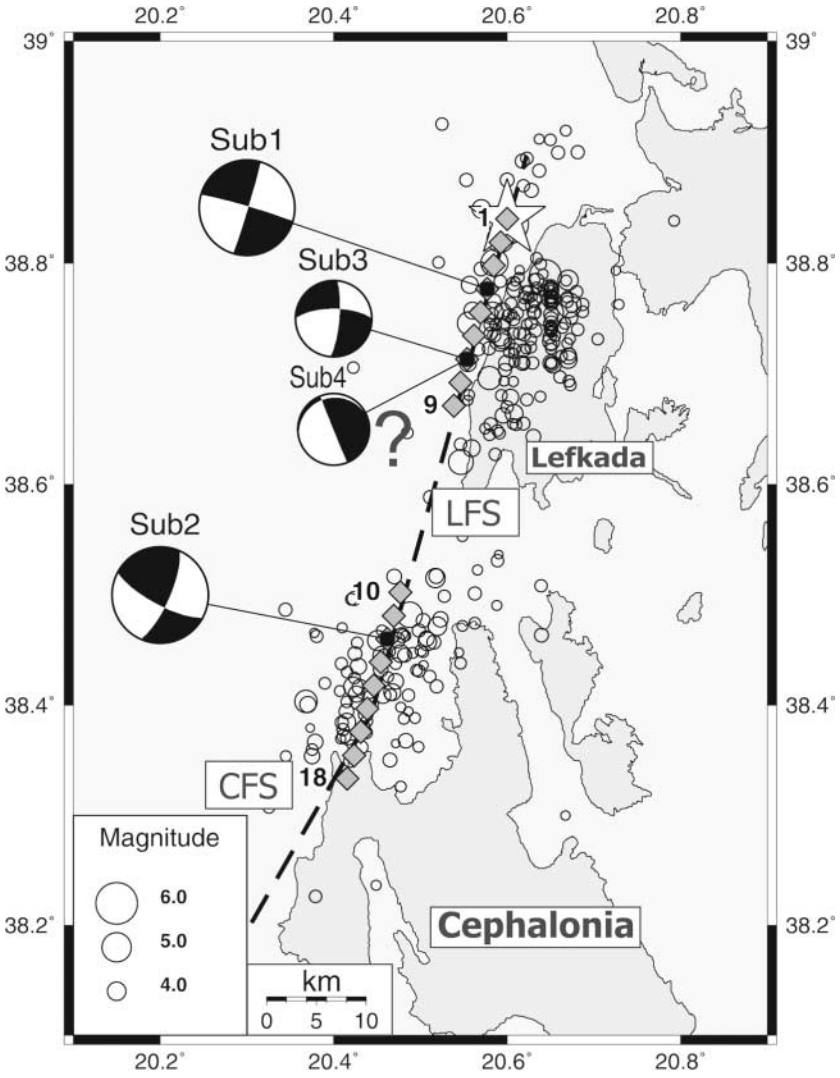

Figure 2. Mainshock (star), aftershocks (circles), trial source positions 1–18 (diamonds), and the resulting four subevents. Shown are the focal mechanisms corresponding to the complete five-station data set (Table 3). The question mark indicates that subevent 4 is the least certain, in terms of the uncertainty estimate of Figures 5 and 7. LFS and CFS are geological names of the faults mentioned in the text. (Ⓔ A color version of this figure is available online at the SSA Web site.)

Table 2
The PATNET Location of the Mainshock in Three Crustal Models (the last one is used in this article)

Crustal Model	Latitude N (°)	Longitude E (°)	Depth (km)
Novotný *et al.* (2001)	38.85	20.65	1
Tselentis *et al.* (1996)	38.83	20.62	16
Haslinger *et al.* (1999)	38.84	20.60	13

strike (e.g., Louvari *et al.* [1999]): the Lefkada Fault Segment (LFS) and the Cephalonia Fault Segment (CFS). Figure 2 shows that the aftershocks are separated into two clusters, close to the northern and southern edges of the LFS.

Most epicenters are situated to the east of the fault, at least in the northern cluster, which indicates its eastward dip. However, inferences regarding the dip angle should be avoided. In fact, as intuitively expected because of the lack of stations west of the epicenter, formal error analysis, based on covariance matrix, showed that the east–west error is about 50% larger than the north–south error. The true foci are probably shifted somewhat to the west, but the absolute value of such a shift remains unknown.

Note: although the two clusters are well separated in space, they operated practically simultaneously. Although it is not easy to identify wave onsets soon after the mainshock, an M 4 aftershock undoubtedly had already occurred at Cephalonia at 05:23:57, that is, 9 minutes after the mainshock at Lefkada. (Ⓔ An animated 3D demonstration of the aftershock distribution is available online at the SSA Web site.)

Method

This article uses the iterative deconvolution of multiple point sources, based on Kikuchi and Kanamori (1991). We inspect a set of predefined point-source positions along a line. Once a major point-source contribution (subevent) is found, the corresponding synthetics are subtracted from data, the residual waveform is inverted for another point

source, and so on. Because the optimum source position of each subevent is also to be retrieved, the technique is nonlinear. However, because the point sources are removed consecutively, one after another, each step has only two parameters (source position and onset time), thus contributing to the stability of the inversion. The remaining part, that is, the deviatoric moment tensor inversion, is linear, but again with a low number of parameters, just five tensor components. We have newly encoded this technique to allow full wavefield modeling at regional (and local) distances, based on the discrete wavenumber method of Bouchon (1981) and Coutant (1989).

When seeking the subevents, their moment rate has a predefined shape and duration. If shorter than the least studied period, it is formally represented by the delta function (as in this article). The moment tensors of the subevents are retrieved by minimizing L2 misfit between records and synthetics, solving normal equations. The inverse matrix provides formal variance of the moment tensor components, showing how the individual tensor components are resolved with respect to each other and/or warning about the ill-conditioned inversion. To get a more useful error estimate, reflecting uncertainties due to crustal structure, several artificially generated data (data subsets) should be studied, and that is our favorite approach.

The optimum subevent position and time are found by a grid search, in which we maximize correlation between observed and synthetic waveforms. For simplicity and speed, we use the correlation coefficient, indirectly obtained during the least-squares minimization (see equations 6 and 11 of Kikuchi and Kanamori [1991]). The grid search is nonunique. Therefore, again following the referenced article, we plot the correlation between observed and synthetic waveforms as a 2D function of the source position and time, also showing the focal mechanism at all trial subevent positions. Such a graphic tool (see Fig. 3) allows an interactive control of the "subevents walk" through space and time. In this way we can also apply various constraints. For example, we may prefer focal mechanisms that agree with first-motion polarities, as demonstrated later.

Parallel to the DC-unconstrained moment tensor inversion, we also run a DC-constrained inversion, using Lagrange multipliers. We use equations 9a and 9b of Kikuchi and Kanamori (1991). The constraint is nonlinear; it is applied iteratively. In the first approximation, the determinant and its partial derivatives are evaluated at the best-DC part of the unconstrained moment tensor. To terminate the iteration process we request the DC percentage to be between 90% and 100% and, simultaneously, the correlation to not be worse than 50% of the correlation value of the nonconstrained solution.

Fit between the resulting data and synthetics is measured by the variance reduction, defined as $varred = 1. - (|residual|/|data|)$. Here $|.|$ denotes the L2 norm, that is, the squared amplitudes, summed over time, components, and stations; and $residual = data - synthetics$. If a filter is used, it is assumed that it is applied to both the data and synthetics. Then, *varred. 100* can be understood as percentage of data power explained by the model. It is useful to calculate *varred* after retrieval of each subevent. As the subevents are consecutively removed, the *varred* increases. It is not easy *a priori* to set up a threshold value of *varred* at which the calculation should terminate, because *varred* values depend on the size of data set and also on the maximum frequency under study. Therefore, we should look not only at the *varred* value but also at its change. As a rule, the first few largest subevents increase the variance reduction very quickly, then the increase becomes slow, and we observe a kind of "convergence," indicating that additional subevents are not needed (cannot be resolved). However, as shown later, a stronger criterion is to be applied when deciding whether to add another subevent or to stop the inversion. Such a criterion is stability. (By subevent stability we mean that its position, time, and mechanism remain similar when perturbing or reducing the data set.) Unstable subevents cannot be accepted even if they still formally increase *varred*.

Data and Preliminary Tests

Five nearest broadband stations were selected for the waveform modeling (Fig. 1). Four stations (KEK, JAN, EVR, and RLS) belong to the National Observatory of Athens, Institute of Geodynamics (NOA-IG). One station (SER) is jointly operated by the Charles University, Prague, and the University of Patras. The NOA stations are equipped by Lennartz 20-s sensors, whereas SER has a Guralp 100-s sensor. The SER records are available at http://seis30.karlov.mff.cuni.cz.

The velocity records were bandpass filtered between 0.05 and 0.1 Hz, instrumentally corrected, and integrated to displacement. The studied time window was 200 s, starting at the hypocentral time. It may be useful to mention that a few tests in a broader frequency range, 0.05–1.0 Hz, provided very similar results (concerning the position and focal mechanism of the two main subevents). Obviously, with the simple crustal model, the variance reduction was much worse, so hereafter we stay at less than 0.1 Hz.

The periods 10 to 20 s, and the relatively small epicentral distances (<140 km), enable some insight into the source process. At the same time, knowledge of the crustal structure is sufficient at those periods. We proved the latter by successful point-source forward modeling of a M 5 aftershock (14 August at 16:18 UTC). The Lefkada mainshock was also subjected to a preliminary single point-source forward modeling, but the agreement with data was very poor, thus indicating the importance of the finite source extent.

In our preliminary analysis of the Lefkada earthquake, nine trial-source positions were used, with the spacing of 10 km, distributed along a straight line passing through the epicenter (Zahradník *et al.* [2003], unpublished report posted on the EMSC Web page [http://www.emsc-csem.org/]). Two major source positions were identified, one at Lefkada

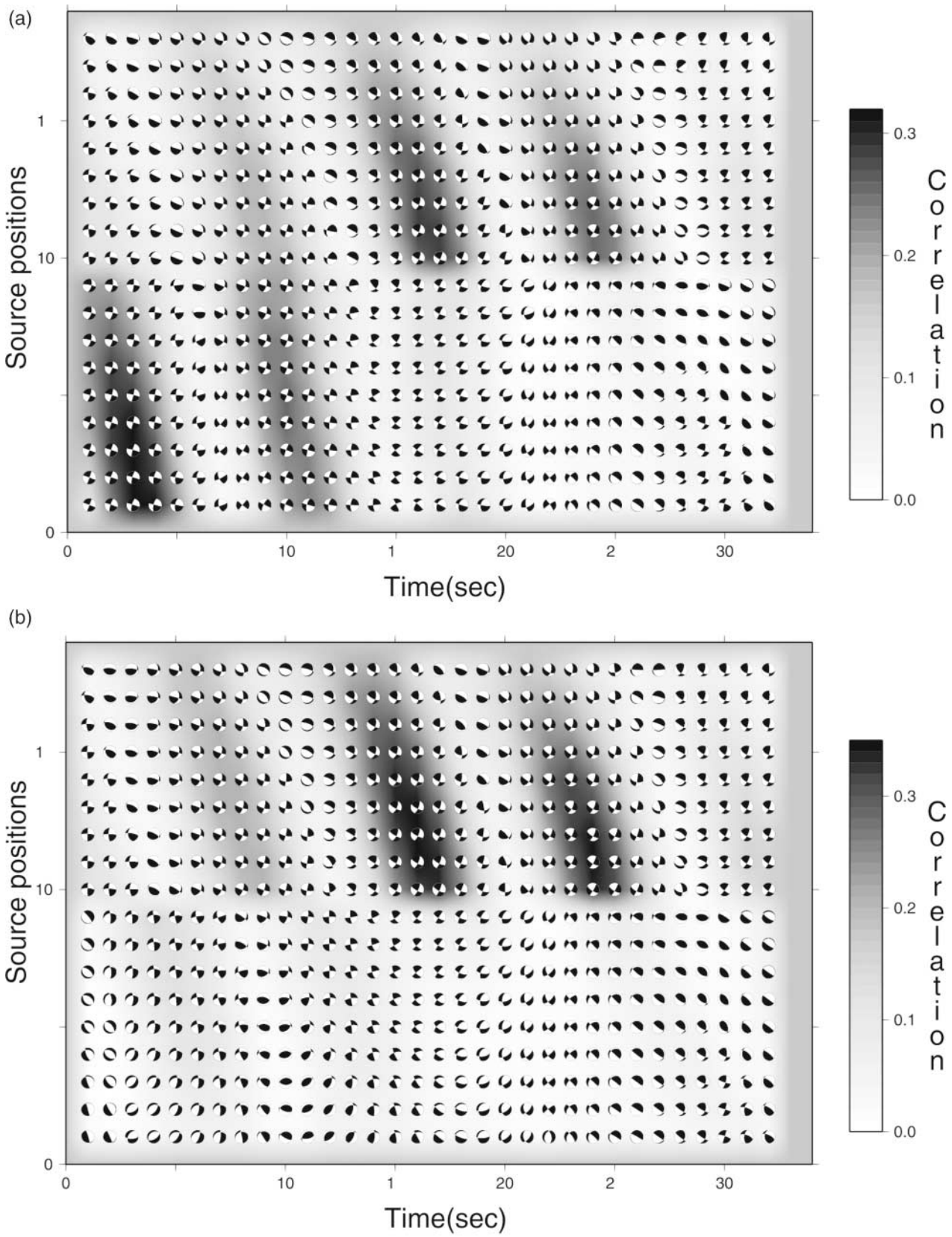

Figure 3. (a) A 2D correlation plot to find position and time of subevent 1. Note a discontinuity between trial positions 9 and 10, which are separated by 20 km. (b) A 2D correlation plot to find position and time of subevent 2. Note a discontinuity between trial positions 9 and 10, which are separated by 20 km. (Ⓔ A color version of this figure is available online at the SSA Web site.)

and the other at Cephalonia, 40 km from each other. As a next step, a long series of tests was performed to check the effect of varying the position of the source line, depth of the source line, and the crustal model. Basically, in the following text we focus only on the robust results, practically independent of these variations. Specifically, as previously mentioned, the inversion reported here is based on the crustal model of Haslinger *et al.* (1999), and the line of trial sources is situated at the hypocenter depth of 13 km (Table 2).

Another important issue is the reliability of the moment tensor inversion regarding its double-couple (DC) part, and the non-DC part, respectively. In all cases tested (hundreds of tests) we found that coming through the regions of the highest 2D correlation of the DC-unconstrained inversion, there were closely spaced solutions whose best-DC mechanisms differed by a few degrees in strike, dip, and rake, but their DC percentage varied as much as 40% to 90%. This common behavior was understood as a strong indication that the non-DC part (CLVD) is an artifact. Note that with a plain least-squares inversion, without the correlation analysis, it would be much more difficult to recognize the false non-DC solutions. Moreover, in our data set, the DC-constrained solution is very close to the best-DC part of the unconstrained solution. Specifically, their deviation is much smaller than the deviations introduced by artificially perturbing the data set. At the same time, we found that the DC constraint has negligible effect (about 1%) on the resulting variance reduction. If a non-DC component exists, it cannot be resolved with the available data. For all these reasons, we present only the best-DC part of the DC-constrained solution, not the complete moment tensor.

Results

Subevents 1 and 2

This study started with the following setup of the trial source positions: 15 trial source positions were distributed along a straight line at the depth of 13 km, striking N20° E, and passing through the hypocenter (38.84° N, 20.60° E). It extended 10 km to the north from the hypocenter, and 60 km to the south, without any gap, and had 5 km spacing between the trial positions. Ten subevents were formally retrieved. The largest two occurred 10 and 45 km from the hypocenter (toward the south). All the other subevents had their moment smaller than one half of subevent 1 or 2. None of them occurred in the region spanning the interval of 20 to 40 km, measured from the hypocenter toward the south, thus strongly indicating a low slip region there.

Therefore, to make even a more detailed insight into the source process, hereafter we focus on another setup along the same line, that is, 18 trial point-source positions, 9 at Lefkada and 9 in Cephalonia, now with spacing of 2.5 km (see Fig. 2). We emphasize that the idea to leave the 20-km segment between Lefkada and Cephalonia free of the trial source positions is not based on the knowledge of the aftershock clustering. It is nothing but a "zooming" suggested by the previous calculation with the equidistant positions.

To determine the first subevent, we analyze the 2D correlation plot of Figure 3a. Because of limited resolution at $f < 0.1$ Hz, the correlation is not sharply peaked. Anyway, as in the preliminary test, we have a choice between two main source contributions, characterized by nearly the same amount of correlation (see the smooth maxima smeared between source positions 1 to 6 and 10 to 13). Note also that the maxima in Figure 3 are "doubled" along the horizontal time axis, roughly at a half-period distance. This is an undesired consequence of the fact that we work in a relatively narrow frequency band, in which waveforms are close to sinusoidal, so that a half-period shifted function of the opposite sign fits the data equally well. One of the "double" maxima is false and could produce a wrong focal mechanism. For example, fix a source position 4, and move along the time axis from the left to the right. You find the major cloud at time ~3 s, with predominantly right-lateral strike slip, and the other one (with a lower correlation) at time ~10 s, featuring the left-lateral motion. The latter, however, contradicts the first-motion polarities, so we must ignore it. This is how we apply the first-motion polarity constraint. Another, more subtle feature to be mentioned, is the fault dip. The formal global maximum value of the 2D correlation (position 1, time 4 s) indicates a fault dipping to the west, contradicting the aftershock distribution. However, moving to a slightly lower correlation, we easily find the east-dipping solution (position 4, time 2 s), and this is our second, weaker constraint, when retrieving the first subevent. The final solution for the first subevent is in Table 3, and it is also shown by a beach ball in Figure 2.

Now we calculate the corresponding point-source synthetics of the first subevent, remove it from the data, and get a new 2D correlation map (Fig. 3b), representing our starting point for retrieving the second subevent. The formal maximum of correlation at position 12 and the time of 16 s provides a focal mechanism similar to the first subevent (Fig. 2 and Table 3); it is predominantly right-lateral strike slip, but less steeply dipping, and with a small thrust component. There is no reason to apply any additional constraint here. It is perhaps useful to mention that the parameters of subevents 1 and 2 are almost independent of their retrieval succession; that is, we could equally well start with removing a subevent at position 12 and then automatically obtain the next one at position 4.

Let us also mention that, comparing with the previously discussed experiment with the 15 equidistant source positions, the major source contributions are now practically the same. Indeed, with the present step of 2.5 km, subevent 1 is only 2.5 km apart from its position in the previous test (where the step of 5 km was used), with a corresponding change of the dip and rake by 5° and 2°, respectively. Subevent 2 is identical with the one from the 15-position test. Seismic moment and timing of both subevents 1 and 2 are the same as in the 15-position test, too. Independence of the

Table 3
Source Parameters of the Four Retrieved Subevents

Moment (10^{18} N m)	Strike (°)	Dip (°)	Rake (°)	*Varred* (×100) (%)	Omitted Station
Subevent 1: position 4, time 2 s					
.47	**17**	**88**	**−177**	**29**	**None**
.54	15	86	−178	33	JAN
.48	20	87	−172	29	EVR
.55	23	86	−178	37	RLS
.50	12	86	−178	34	KEK
.32	198	75	−168	15	SER
Subevent 2: position 12, time 16 s					
.49	**24**	**74**	**164**	**54**	**None**
.46	22	70	161	54	JAN
.57	27	70	162	60	EVR
.52	25	75	167	57	RLS
.46	21	81	168	60	KEK
.44	26	72	163	42	SER
Subevent 3: position 7, time 5 s					
.23	**5**	**78**	**−159**	**61**	**None**
.25	8	80	−162	62	JAN
.23	1	82	−146	66	EVR
.25	9	76	−157	65	RLS
.21	7	58	175	66	KEK
.20	360	84	−162	48	SER
Subevent 4: position 7, time 26 s					
.19	**158**	**89**	**103**	**66**	**None**
.29	133	78	118	70	JAN
.18	145	67	143	68	EVR
.19	176	88	91	70	RLS
.17	325	85	−86	70	KEK
.21	341	89	−105	54	SER

It is the best-DC part of the DC-constrained moment tensor. Position refers to the trial numbers 1–18 of Figure 2. Time is relative with respect to the hypocentral time. The variance reduction is denoted *varred*. Highlighted rows correspond to the five-station solution, whereas the other rows are for the four-station reduced data sets (created by successively omitting one station, as indicated in the last column). The reduced data set provides the uncertainty estimate. See also Figures 5 and 7.

step size (5 or 2.5 km) is related to the relatively long periods (10 to 20 s) and the relatively large fault lengths of subevents 1 and 2 (see later in the paragraph on the fault segmentation).

It is useful to demonstrate the waveform contribution of the two main subevents. With subevent 1 only, major late phases remain unexplained, for example, at SER-NS, JAN-EW, RLS-NS. Also the *Z* component is too small at SER and JAN, and the variance reduction is only 29%. The summed subevents 1 and 2 basically remove these problems, and the variance reduction increases to 54%. Figure 4 illustrates these effects for two stations, SER and JAN.

Partial conclusion is that two subevents (Lefkada and Cephalonia) explain the data better than a single event close to the epicenter (Lefkada), and this result is in a good agreement with the two aftershock clusters.

The two subevents cannot be easily recognized in the nonfiltered records. The problem is that at all stations, except RLS and SER, the second subevent arrives within the *S*-wave group of the first subevent. In RLS and SER records, there are indeed several prominent arrivals between the first *P* onset and the *S* onset, but it is not possible to unambiguously relate two of them with the first and second subevents. That is why figures like that are not presented here.

To estimate uncertainty, we use five reduced data sets, each one generated by removal of one of the five stations. A procedure like that is suggested by the fact that the weakest point of our method is the 1D crustal model, inherently unable to reflect any variation from one source-station path to the other. Therefore, changes of the solution due to inclusion or omission of a station can easily be large. If they are small, it is a strong indication of a robust result. On the other hand, with these few stations we can not generate a large artificial data set to understand the statistical distribution of the parameters and to quantify the confidence intervals. An alternative strategy might be to build up very large artificial data sets by more delicate perturbations, For example, by omitting some samples from the time series. It would produce a statistical distribution of the parameters, but its physical meaning is doubtful (there is no physics behind an omitted sample), and the standard deviation would be very small (e.g., smaller than that obtained by comparing source parameter reports from several agencies). In a situation like that, and because we mainly aim at understanding the relative robustness of the individual subevents, we prefer the station elimination check.

Before repeatedly inverting the reduced four-station data sets, we fix the position and time of the first two subevents, found from the five-station data set (positions 4 and 12, times 2 and 16 s, respectively). Then we retrieve their DC-constrained moment tensors. As seen from Fig. 5, showing the composite plot of all nodal lines, and from Table 3, both subevents 1 and 2 have a very stable (well resolved) focal mechanism. This indicates that the reduced data sets are consistent with the fixed position and time. In other words, the fixing is natural. This was also independently checked by repeating the inversion for the reduced data sets while making the subevent position and time free. Indeed, positions 4 and 12 were always strongly suggested. The time of 16 s for subevent 2 was always characterized by a high correlation and by the right-lateral strike slip. It was automatically obtained as a formal maximum in most of the reduced data sets. However, in two of them (when omitting SER or KEK), the formal maximum of correlation for subevent 2 occurred at 24 s, and the preferred mechanism was a left-lateral strike slip.

A small comment needs to be made regarding subevent 1 retrieval, with omission of the SER station, because it has the smallest value of *varred*, only 15% (see Table 3). It may cause speculation about the specific role of the SER instrument and/or a site effect. Although the SER instrument is indeed different from the other stations, it provides the least likely explanation, because at all stations we study the period range 10 to 20 s only. The site effect is also not likely because the SER station does not exhibit a singular behavior

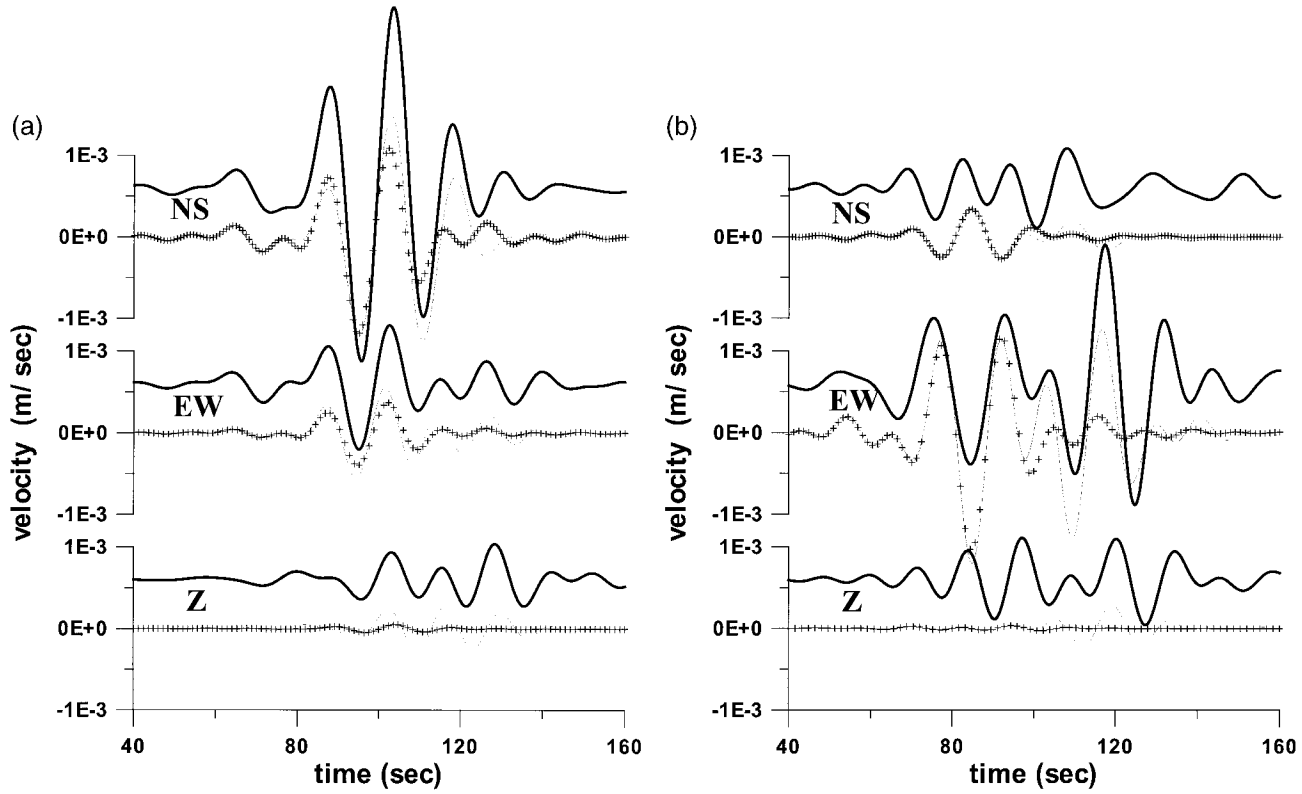

Figure 4. (a) Station SER. Records (top) and synthetics (bottom) for subevent 1 (crosses), and for summed subevents 1 + 2 (solid line). (b) Station JAN. Records (top) and synthetics (bottom) for subevent 1 (crosses), and for summed subevents 1 + 2 (solid line). NS, north–south; EW, east–west. (Ⓔ A color version of this figure is available online at the SSA Web site.)

systematically for all earthquakes. For any earthquake we may find a station whose behavior is substantially different from the other stations. It is related in a complex manner to the spatial distribution of the stations with respect to the source and its focal mechanism. The specific feature of the SER record of the 2003 Lefkada earthquake is that SER-NS has the largest amplitude of the entire data set. The next two dominant waveforms are JAN-EW and RLS-NS, (see Fig. 8). As such, the presence of the SER record in the inverted data set strongly controls the solution, providing the major subevent at position 4 (Lefkada). If the SER station is omitted, the dominant waveforms JAN-EW and RLS-NS take the most important role, and their strong late arrivals tend to push the major subevent into position 12 (Cephalonia), time 24, with a left-lateral strike slip, mentioned previously. The artificial constraint of the subevent succession retrieval, position, and time then makes the case of SER omission closer to the other reduced data sets, as seen in Table 3 (the right-lateral strike slip), but the seismic moment and *varred* remain significantly lower. Finally, large amplitudes at SER and JAN come from the positions of these stations on the focal sphere, which are nodal for *P* waves, but, simultaneously, they are located on the plane containing the *P* and *T* axes, where *S* waves are strong.

Subevents 3 and 4

The crucial point is whether to stop inversion at this level or to add some more (weaker) subevents. The answer is conditional. Revealing a few weaker source contributions is possible, but it needs more care. The inherent complication, that is, the inapplicability of the "brute force" automatic approach, is demonstrated in Figure 6. In that case we adopted subevents 1 and 2 as shown in Table 3 and inverted the residual seismograms for subevents 3 and 4 quite automatically, that is, following the formal correlation maxima, without fixing any position and time. In contrast to subevents 1 and 2, the inversion suggested several source positions, strongly varying from one reduced data set to the other, mainly for subevent 4. Consequently, the focal mechanisms were also unstable, as shown in Fig. 6.

Therefore, we keep in mind that the exact positions and times of subevents 3 and 4 are unresolved; nevertheless, we still might be interested in some estimation of their focal mechanisms. To that goal we artificially fix the positions and times of subevents 3 and 4. First, before fixing the position, we analyze the five-station data set in more detail. Regarding subevent 3, the formal maximum of the correlation suggested its position is 9 at a time of 4 s. However, compared with the neighboring subevent 1 at position 4, spaced by

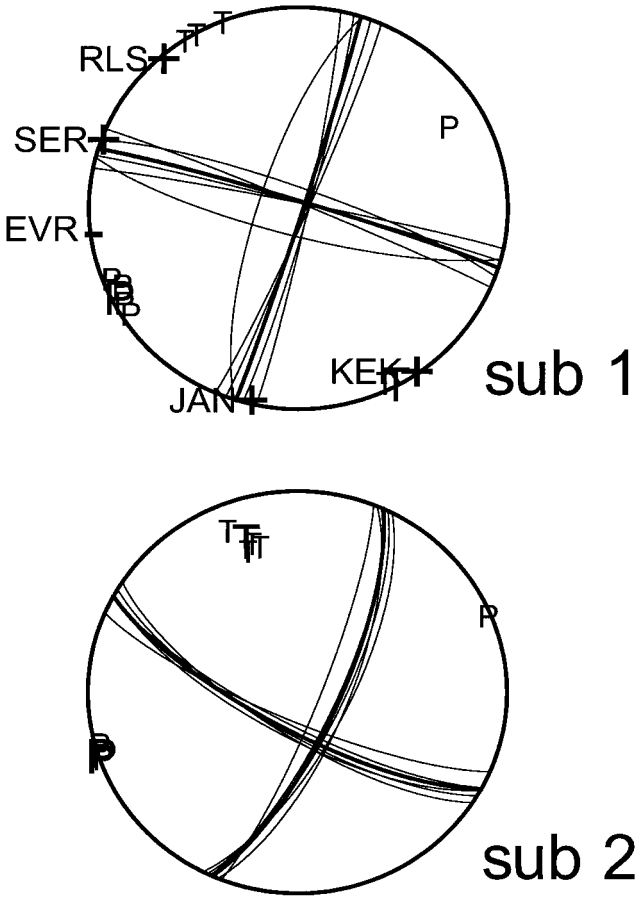

Figure 5. The uncertainty analysis for subevent 1 (top) and subevent 2 (bottom). (top) The observed first-motion polarities are also shown. The highlighted solution is for the complete five-station data set, whereas the others are for the reduced four-station sets. (Ⓔ A color version of this figure is available online at the SSA Web site.)

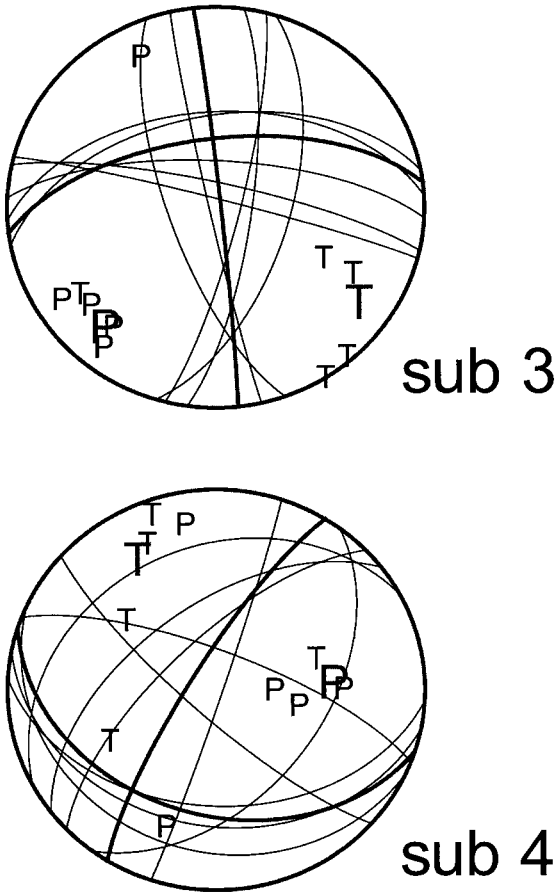

Figure 6. The preliminary uncertainty analysis for subevent 3 (top) and subevent 4 (bottom). The solution is unstable mainly because of variation of the subevent source position and time. (Ⓔ A color version of this figure is available online at the SSA Web site.)

12.5 km, such a solution would imply a nonrealistic rupture speed. Therefore, a constraint must be applied. As a compromise, we adopted a nearby solution providing a reasonable speed, and the correlation was only a bit worse: position 7 and a time of 5 s. By using these parameters for subevent 3, subevent 4 then gets its reasonable position 7 and a time of 26 s directly, as suggested by the formal correlation maximum. Therefore, we fix both subevents 3 and 4 at position 7, at time of 5 and 26 s, respectively, and proceed to the reduced data sets. As a result, in Figure 7 we get a more stable estimate of the focal mechanism than that in Figure 6. In any case, compared with subevents 1 and 2, it is obvious that the uncertainty increases. Note also (Table 3) that the variance reduction still grows, but slowly.

A partial conclusion is that subevents 3 and 4 represent later rupture episodes spatially close to subevent 1, with different focal mechanisms. Although the uncertainty is large (mainly for subevent 4), the indication of the spatially nonuniform focal mechanism is strong. The complexity of the rupture process is also independently supported by the other experiments, not presented here, in which all attempts to explain the whole earthquake with an extended model of single (fixed) focal mechanism clearly failed.

Figure 8 compares data with synthetics, including the four retrieved subevents. To reflect the uncertainty, the whole family of synthetic seismograms is plotted, corresponding to the inversion of all six data sets of Table 3. The final value of the variation reduction is 70%, or less, depending on the reduced data set. Formal continuation of the inversion process with five more subevents would still (but very slowly) increase *varred*, but not more than up to about 80%, and the uncertainty would also grow further. In other words, the complete five-station data set and a 1D crustal model do not contain consistent information about more source details. Some tests with further reduced data sets, including as few as two to three stations, indicated a possible additional subevent at Cephalonia and one situated to the north of the epicenter at Lefkada. The latter not only partially explained a small aftershock cloud there, but it also im-

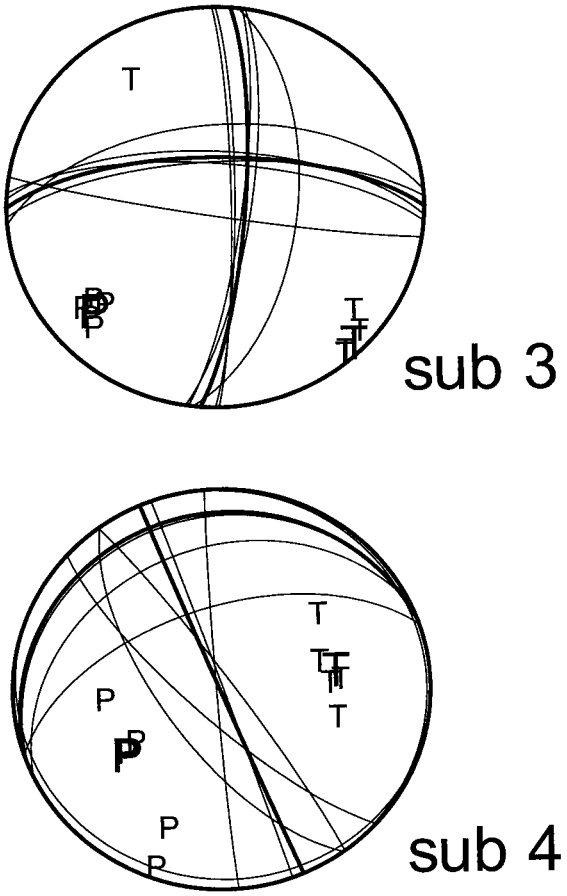

Figure 7. The final uncertainty analysis for subevent 3 (top) and subevent 4 (bottom). The solution was artificially stabilized by keeping the subevent positions and time fixed at their values obtained with the full five-station data set. (Ⓔ A color version of this figure is available online at the SSA Web site.)

proved simulation of the strong late phases at the KEK station. However, the uncertainty was large. Therefore, we terminate the inversion with subevent 4. Nevertheless, we bear in mind an unexplained part of data power, which might indicate an unrevealed amount of slip, and we return to this issue later when discussing the fault size.

Speaking about the larger uncertainty of subevents 3 and 4 compared with 1 and 2, it is important to note that subevents 3 and 4 are relatively small. It is documented not only by their moments (Table 3), but also by Figure 9, corresponding to the five-station inversion. Indeed, compared with Figure 4, where the difference between one and two subevents was great, Figure 9 shows that the difference between two and four subevents is much smaller, although not negligible. At this moment, we must decide whether to conclude that the earthquake can be described by the predominant and best-resolved part of the solution, that is, subevents 1 and 2, or that it should be described by (at least) four subevents. Obviously, there is no unique objective answer, because it depends on the adopted point of view. We prefer to present four subevents for two reasons: Presenting only the first two (well-resolved) subevents would hide that there also exists a small but less certain additional complexity of the source, not well resolved with the available data. Moreover, presenting only the two largest subevents would too greatly underestimate the total moment.

The Source Segmentation

Before concluding and releasing the results for any further use, for example, for tectonic interpretation, for the Coulomb stress analysis, for strong-motion simulations, etc., the individual features of the solution should be (at least qualitatively) classified regarding their robustness.

1. The most robust feature is concentration of the moment release in two source segments (or events). The northern segment, at Lefkada, is represented by subevents 1, 3, and 4, whereas the southern one, at Cephalonia, is represented by subevent 2. The whole fault length, measured from the hypocenter (source position 1) up to the most distant subevent 2 is 45 km. These robust source features are sufficient to basically explain the two major aftershock clouds.
2. Another robust feature is the focal mechanism of subevents 1 and 2. Both can be characterized as predominantly right-lateral strike-slip motion, but they are not identical.
3. The least robust feature is the positions, times, and focal mechanisms of subevent 3 and (mainly) subevent 4.

The term "segment" as used in our source inversion has nothing to do with the geological names, such as the Lefkada Fault Segment (LFS), or the Cephalonia Fault Segment (CFS). According to Figure 2, both source segments (at Lefkada and Cephalonia) correspond to LFS, not to CFS. However, in this article, such a statement has a merely formal meaning because we do not study the geological distinction between LFS and CFS.

The last remaining issue is to discuss possible fault size. First, assume that the Lefkada 2003 earthquake was a single earthquake, with a heterogeneous slip distribution, and a total fault length of 45 km. Considering the four subevents together, we get a total scalar moment (five-station solution) of 1.4×10^{18} N m, hence M_w 6.1. This is a lower moment than that reported by major agencies (Table 1). Two explanations are possible. Increasing the source depth (to 20–30 km) would increase the moment to about 2×10^{18} N m, M_w 6.2, closer to the other estimates of Table 1, but it would be less compatible with our location results. An alternative explanation appears to be indicated by the fact that our model did not explain the data completely (the fifth and higher subevents were not included because of their low reliability). If it means that subevents 1–4 are the main asperities, we can estimate the total earthquake size as follows: Denote by Moa, Aa, and Da the moment, rupture area, and the average slip on the asperities, and keep symbols Mo, A,

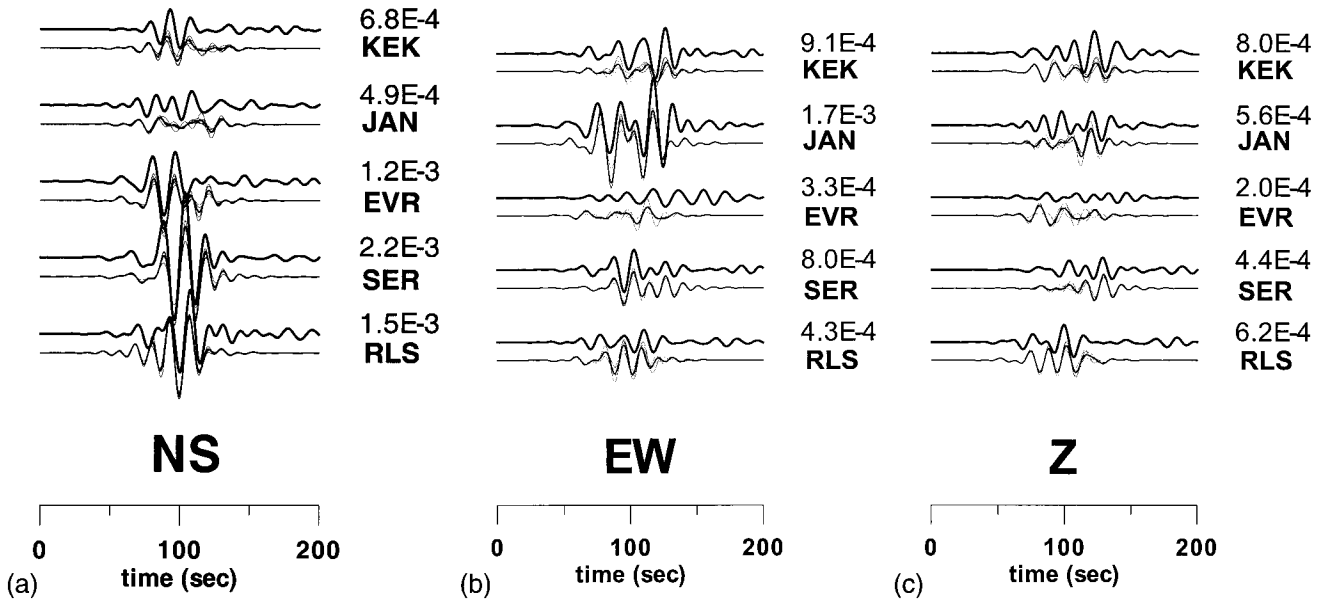

Figure 8. Observed (top) and synthetic (bottom) band-passed velocity waveforms for summed subevents 1 to 4. The peak values (m/s) are shown above the station codes. The whole family of synthetics is shown to reflect the uncertainty, as estimated by means of reduced (four-station) data sets. The synthetic data corresponding to the five-station solution are shown by the thicker line. Panels a, b, and c refer to the north–south (NS), east–west (EW), and *Z* components, respectively. (Ⓔ A color version of this figure is available online at the SSA Web site.)

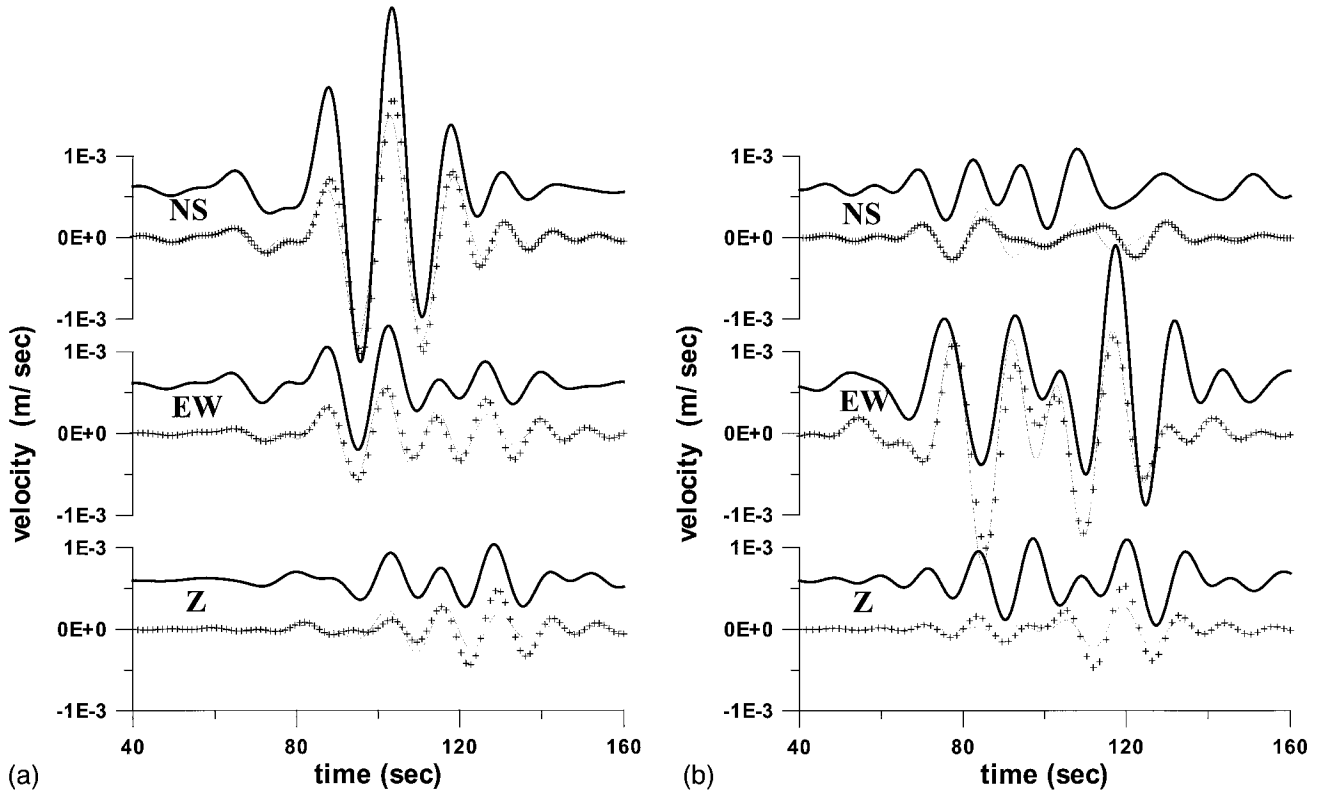

Figure 9. (a) Station SER. Records (top) and synthetics (bottom) for the sum of all four subevents (crosses), and for the subevents 1 + 2 only (solid line). (b) Station JAN. Records (top) and synthetics (bottom) for the sum of all four subevents (crosses), and for the subevents 1 + 2 only (solid line). (Ⓔ A color version of this figure is available online at the SSA Web site.)

and D denoting the corresponding quantities for the whole earthquake. Somerville *et al.* (1999) suggested empirical relations Aa/A = 0.22 and Da/D = 2, from which it follows that Moa/Mo = 0.44. If the total moment of asperities is that of the four subevents, Moa = 1.4×10^{18} N m, we arrive at the whole moment of Mo = 3.2×10^{18} (i.e., M_w 6.3), in agreement with Table 1. Thus we obtained the moment magnitude M_w ranging between 6.1 and 6.3.

However, whatever of this moment estimation is true, according to empirical relations of Papazachos and Papazachou (1997), the fault length of 45 km would be too large for a single shallow earthquake of this magnitude in Greece. Therefore, we suggest the double-event interpretation, with the ruptures of the northern source segment at Lefkada Island (subevents 1, 3, and 4) and the southern segment at Cephalonia Island (subevent 2) considered as *two* earthquakes.

Therefore, if the preceding ideas are separately applied to the two segments, we get a finite-extent (speculative) model as follows: For the Lefkada segment, represented by subevents 1, 3, and 4, the calculated moment is 0.9×10^{18} N m. If it is the total moment of the Lefkada asperities, Moa, the entire Lefkada moment is Mo = 2.0×10^{18} N m. Somerville *et al.* (1999) then implies $A = 164$ km^2. Assuming further, for simplicity, that the segment length is roughly twice as large as its width, we arrive at a 18 × 9 km hypothetical model of the Lefkada segment. Analogously, for the Cephalonia segment represented by subevent 2 (Moa = 0.5×10^{18} N m) we get Mo = 1.1×10^{18} N m, and $A = 110$ km^2, which may have a size of 15 × 7.5 km. The estimated fault lengths are in agreement with the observed aftershock distribution. Finally, using the previous relation Aa/A = 0.22 for three asperities at Lefkada, and one asperity at Cephalonia, we estimate each asperity size as, approximately, 4 × 4 km. Although a similar asperity model explained the observed strong ground motions of the 1999 Athens earthquake (Zahradník and Tselentis, 2002), here it is nothing but a working hypothesis for subsequent studies.

Our next goal is to start from the framework of the source model presented previously, simulate rupture of the asperities, and try to understand the strong ground motions. This study will need a separate article, not only because strong-motion data in Greece are not routinely available on the Internet, but also because the use of higher frequencies will require a completely different approach (empirical Green functions).

The segmented rupture of this earthquake (i.e., a multiple-event explanation) was independently suggested also by Benetatos *et al.* (2005), based on teleseismic data. Karakostas *et al.* (2004) made inferences about the Coulomb stress transfer but considered a single-source segment (Lefkada) only. Implicit support of the segmented source comes also from Harvard Centroid Moment Tensor analysis, providing the 13.5-s difference between the centroid time and hypocentral time, which is unusually large for $M_w < 6.3$.

Speaking of the Harvard solution, it is useful to also mention its nonshear component (DC = 96%, CLVD = 4%). If we consider our 100% DC solutions of the major subevents 1 and 2, and formally sum up their moment tensors, we get a similar nonshear mechanism (DC = 92%). It demonstrates how spurious non-DC mechanisms can appear in relatively long-period studies when complex sources are considered in the point-source approximation.

Conclusions

The moment tensor inversion for multiple point sources, based on Kikuchi and Kanamori (1991), was extended to the full waveform data at regional (or local) distances, using the discrete wavenumber method of Bouchon (1981) and Coutant (1989). The method was newly encoded, and numerous tests resulted in the following methodical messages.

Convergence of the variance reduction is an insufficient criterion to stop the inversion process. Additionally, it is used to check the relative robustness of the subsequent retrieval of the subevents and to terminate the inversion when the uncertainty is large. The problem of "what is large" is open, because it is not possible to construct any large, physically meaningful artificial data sets providing the parameter distribution and confidence intervals. Therefore, judgment about the termination of the inversion remains subjective.

It is also subjective whether to require stability of all subevent parameters (their position, time, and focal mechanism) or only some of them. Fixing some of the parameters serves a helpful constraint to reveal the remaining ones. A strategy like this is advisable when we try to learn as much as possible from a limited data set. On the other hand, if the method is used as an intermediate step between routine point-source moment tensor inversion and a detailed finite-extent source analysis, then a more stringent rejection of uncertain features is preferable. For example, leaving only subevents 1 and 2 in this article would already provide a reasonable first approximation of a finite-extent source model.

Stopping inversion because of increasing uncertainty leaves some data power unexplained (e.g., in this article the variance reduction was not larger than 70%). Therefore, before interpreting the results, for example, compared with the aftershock distribution, one has to remember that only the major moment release was addressed, so the true source may be larger and more complex than reflected by the retrieved subevents.

The iterative deconvolution is a dangerous tool for those users who intend to use it mechanically; the code will nearly always provide "some" solution, which, however, can be completely misleading. For example, in this article, if we omit some station(s) and work less carefully with the 2D correlation, we may erroneously report the left-lateral strike slip or the non-DC part (CLVD) as large as 50%. On the other hand, for those using the method as a delicate tool, it may be rewarding. They will appreciate that very few parameters are searched simultaneously at each step, hence suffering

little from the trade-off. They will also like that the method works as a "transparent box," where effects of various constraints can be clearly seen. And, perhaps most importantly, the user may stop inversion after a few first subevents, save the resulting residual waveforms, and continue under different conditions (e.g., with different trial source positions, free or fixed positions, with or without DC constraint, etc.). Obviously, all these advantages can be used fully when the method is carefully applied to a few selected earthquakes rather than automatically used with massive data sets.

The new code proved to be efficient for retrieving some source complexities of the 2003 Lefkada, Greece, earthquake. The source model was derived from five three-component waveform data at regional distances <140 km, and periods of 10–20 s. The model is summarized in Table 3. The source process commenced by a weak ("first-motion") rupture nucleation at the hypocenter, followed after some 2 s by the first significant moment release of 0.47×10^{18} N m at a distance of 7.5 km to the south-southwest (measured along the trial source line of Fig. 2). Two smaller rupture episodes of about 0.2×10^{18} N m occurred nearby (some 7.5 km to the south-southwest from the first one), still in the Lefkada region, with a delay about 3 and 24 s, respectively. The three episodes (subevents 1, 3, and 4) may represent asperities of the Lefkada source segment. As soon as 14 s later, and 37.5 km to the south-southwest (measured from the first Lefkada subevent), the activity skipped to the Cephalonia source segment, with its major asperity represented by subevent 2, moment release of 0.49×10^{18} N m.

According to formal classification (Fig. 2), both these source segments correspond to the same fault, namely, LFS, but remember that no geological aspects have been studied in this article.

The inversion revealed a nonuniform rupture process, not only regarding its space-time development, but also regarding the focal mechanism. Large deviations from the pure double-couple mechanism were found but interpreted as artifacts. The DC-constrained mechanism is predominantly right-lateral strike slip along a steeply dipping fault of the south-southwest–north-northeast orientation (except subevent 4), but there is a strong indication that each individual subevent had a different focal mechanism (see Table 3 and Figs. 5 and 7).

The uncertainty estimates, obtained from reduced data sets (repeatedly removing one from five stations), show that subevents 1 and 2 are much better resolved than subevents 3 and 4. Two viewpoints on the result are possible. (1) We are not sure of the exact positions and times of subevents 3 and (mainly) 4, but, when artificially fixing their positions and times, we get some estimate of their focal mechanism and moment. Or (2), because the exact positions and times of subevents 3 and (mainly) 4, are not known, we reject subevents 3 and 4, at all. Most importantly, whatever decision is made, there are still two comparably strong, and highly certain subevents 1 and 2, which, without any doubt, prove the segmented (double-event) nature of the studied earthquake and explain the two major aftershock clusters at the Lefkada and Cephalonia Islands.

More details can be obtained with empirical Green's function methods, strong-motion data, etc., but it was interesting to study in this article the limited resolution of the mainshock data from the regional broadband network, because such data are often immediately available.

An interesting task calling for a separate study is the question of what physics (e.g., a triggering) was behind the double-event nature of this interesting earthquake. And what are the Coulomb-stress implications of such a segmented earthquake for future events in the Ionian region. In fact, the studied 14 August earthquake has already been followed by another nearby event (M 5 earthquake on 16 November 2003, 07:22 at Cephalonia, latitude 38.28° N, longitude 20.38° E), and we should ask whether its position might have been more "predictable" when taking into account the double-event nature of the 14 August event.

The program package developed in connection with this article is called ISOLA, to emphasize the focus on the Isolated Asperities. The package, consisting of a Fortran code (J.Z.) and Matlab graphic user interface (E.S.), is available on request.

Acknowledgments

The authors thank Dr. George Stavrakakis, the NOA-IG director, for kindly providing the broadband seismograms. The GMT software of P. Wessel and W. Smith was used. This work was supported by Czech Research Projects MSM 113200004 and GACR 205/03/1047 and by EC Project EVG3-CT-2002-80006 (MAGMA).

References

Benetatos, Ch., A. Kiratzi, Z. Roumelioti, G. Stavrakakis, G. Drakatos, and I. Latoussakis (2005). The 14 August 2003 Lefkada Island (Greece) earthquake: focal mechanisms of the mainshock and of the aftershock sequence (in press).

Bouchon, M. (1981). A simple method to calculate Green's functions for elastic layered media, *Bull. Seism. Soc. Am.* **71,** 959–971.

Coutant, O. (1989). Program of numerical simulation AXITRA, Research report, Laboratoire de Géophysique Interne et Tectonophysique, Grenoble.

Das, S., and B. V. Kostrov (1990). Inversion for seismic slip rate history and distribution with stabilizing constraints: application of the 1986 Andreanof Islands earthquake, *J. Geophys. Res.* **95,** 6899–6913.

Frankel, A. (2003). Source process of the M7.9 Denali Fault, Alaska, Earthquake: sub-events, directivity, and scaling of high-frequency ground motion (abstract), *EOS Trans. AGU*, **84,** no. 46 (Fall Meet. Suppl.), S11H-03.

Haslinger, F., E. Kissling, J. Ansorge, D. Hatzfeld, E. Papadimitriou, V. Karakostas, K. Makropoulos, H.-G. Kahle, and Y. Peter (1999). 3D crustal structure from local earthquake tomography around the Gulf of Arta (Ionian region, NW Greece), *Tectonophysics* **304,** 201–218.

Karakostas, V. G., E. E. Papadimitriou, and C. B. Papazachos (2004). Properties of the 2003 Lefkada, Ionian Islands, Greece, earthquake seismic sequence and seismicity triggering, *Bull. Seism. Soc. Am.* **94,** 1976–1981.

Kikuchi, M., and H. Kanamori (1991). Inversion of complex body waves. III, *Bull. Seism. Soc. Am.* **81,** 2335–2350.

Kuge, K. (2003). Source modeling using strong-motion waveforms: toward

automated determination of earthquake fault planes and moment release, *Bull. Seism. Soc. Am.* **93,** 639–654.

Lavallee, D., and R. J. Archuleta (2003). Stochastic modeling of slip spatial complexities for the 1979 Imperial Valley, California, earthquake, *Geophys. Res. Lett.* **30,** 49-1–49-4.

Lee, W. H. K., and C. M. Valdés (1989). Hypo71PC.Toolbox for seismic data acquisition, processing, and analysis. International Association of Seismology and Physics of the Earth's Interior (IASPEI) and Seismological Society of America (SSA).

Louvari, E., A. A. Kiratzi, and B. C. Papazachos (1999). The Cephalonia Transform Fault and its extension to western Lefkada Island (Greece), *Tectonophysics* **308,** 223–236.

Novotný, O., J. Zahradník, and G-A. Tselentis (2001). North-western Turkey earthquakes and the crustal structure inferred from surface waves observed in the Corinth Gulf, Greece, *Bull. Seism. Soc. Am.* **91,** 875–879.

Papadimitriou, E. E. (2002). Mode of strong earthquake recurrence in the central Ionian Islands (Greece): possible triggering due to Coulomb stress changes generated by the occurrence of previous strong shocks, *Bull. Seism. Soc. Am.* **92,** 3293–3308.

Papazachos, B. C., and C. B. Papazachou (1997). *The Earthquakes of Greece*, Thessaloniki, Ziti Editions.

Somerville, P., K. Irikura, R. Graves, S. Sawada, D. Wald, N. Abrahamson, Y. Iwasaki, T. Kagawa, N. Smith, and A. Kowada (1999). Characterizing crustal earthquake slip models for the prediction of strong ground motion, *Seism. Res. Lett.* **70,** 59–80.

Tselentis, G.-A., N. S. Melis, E. Sokos, and K. Papatsimpa (1996). The Egion June 15, 1995 (6.2 ML) earthquake, Western Greece, *Pure Appl. Geophys.* **147,** 83–98.

Vallée, M., and M. Bouchon (2004). Imaging coseismic rupture in far field by slip patches, *Geophys. J. Int.* **156,** 615–630.

Zahradník, J., and G.-A. Tselentis (2002). Modeling strong-motion accelerograms by PEXT method, application to the Athens 1999 earthquake, in *Proc. of XXVIII Gen. Assembly of the Europ. Seismol. Commission*, 1–6 September 2002, Genoa, Italy (CD-ROM).

Faculty of Mathematics and Physics
Charles University in Prague
V Holesovickach 2
180 00 Prague, Czech Republic
jz@karel.troja.mff.cuni.cz
(J.Z.)

Seismological Laboratory
University of Patras
261 10 Rio, Greece
(A.S., G.-A.T.)

Institute of Geodynamics
National Observatory of Athens
P.O. Box 20048
118 10 Athens, Greece
(E.S.)

Manuscript received 26 February 2004.